

Cold atom confinement in an all-optical dark ring trap

Spencer E. Olson, Matthew L. Terraciano, Mark Bashkansky, and Fredrik K. Fatemi
Naval Research Laboratory, 4555 Overlook Ave. S.W., Washington, DC 20375

(Dated: July 9, 2021)

We demonstrate confinement of ^{85}Rb atoms in a dark, toroidal optical trap. We use a spatial light modulator to convert a single blue-detuned Gaussian laser beam to a superposition of Laguerre-Gaussian modes that forms a ring-shaped intensity null bounded harmonically in all directions. We measure a $1/e$ spin-relaxation lifetime of ≈ 1.5 seconds for a trap detuning of 4.0 nm. For smaller detunings, a time-dependent relaxation rate is observed. We use these relaxation rate measurements and imaging diagnostics to optimize trap alignment in a programmable manner with the modulator. The results are compared with numerical simulations.

PACS numbers: 32.80.Pj, 39.25.+k, 03.75.Be

Toroidal traps for cold atoms have recently been of interest for both fundamental and applied research. A toroidal geometry can enable studies of phenomena in non-simply connected or low dimensional topologies [1, 2, 3, 4, 5, 6, 7, 8, 9, 10, 11, 12], *e.g.* superfluid persistent circulation states of Bose-Einstein condensates (BECs) [1]. A ring-shaped atom waveguide may also be suitable for inertial measurements [13] and neutral atom storage [9, 10, 11, 14].

Several approaches for generating ring-shaped waveguides have been proposed and implemented. Magnetic fields have been used to create large ring traps for possible use as atom storage rings or Sagnac interferometry [2, 10, 11, 14]. Helmerston *et al.* [1] used a combination of magnetic and optical fields to demonstrate persistent current flow of a BEC. Morizot *et al.* [8] proposed ring traps formed from the combination of an optical standing wave with rf-dressed atoms in a magnetic trap.

All-optical approaches have also been considered for toroidal traps [15, 16, 17]. Wright *et al.* [15] suggested the use of high-azimuthal-order Laguerre-Gaussian (LG) beams to confine atoms with red-detuning. Atoms in red-detuned optical traps seek high intensity, and with large detuning, spontaneous photon scattering can be negligible. Photon scattering can also be reduced by using blue-detuned optical traps. Such “dark” traps confine atoms to low intensity, allowing field-free measurements [18, 19, 20, 21], but are challenging to make because they require an intensity minimum bounded by higher intensity. This challenge is often overcome by crossing beams [20, 22, 23] to plug a hollow optical potential, although dark point atom traps have been realized with a single laser beam containing a phase-engineered intensity null [18]. The single beam approach has the advantage of alignment simplicity over crossed-beam configurations. Lattices of dark rings have been proposed [17] and realized [16] using counterpropagating laser beams, but to the best of our knowledge, there have been no reports of atom confinement in a lone optical ring trap.

In this paper, we report atom confinement within a different class of dark optical ring traps. We form a bounded, ring-shaped intensity null by converting a Gaussian laser beam to a dual-ringed beam with a pro-

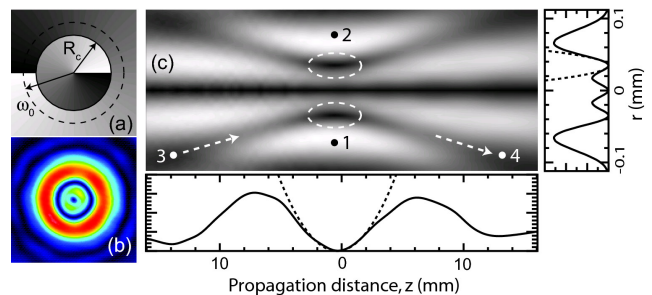


FIG. 1: (Color online) a) Phase profile for creating the dark optical ring. b) CCD image of a dual-ringed beam in the focal plane. c) Numerical simulation of r - z cross section. Right: Transverse profile through the minimum, on a line through points 1 and 2. Bottom: Profile along the minimum-intensity path, indicated by the arrows, through points 3 and 4. Length scales are shown on the profile plots. The dashed curves in the profile plots are quadratic fits. The dark trap is formed in a ring through the centers of the dashed ellipses.

grammable spatial light modulator (SLM). SLMs are of increasing value in cold atom manipulation experiments because of their ability to reconfigure trap parameters [23, 24, 25, 26, 27]. We measure the spin-relaxation lifetime, observe atom dynamics within the traps, and compare the experimental results with numerical simulations.

We form the dual-ringed laser beam by modifying the spatial phase of a laser beam with an SLM, in a similar manner to that used for producing hollow laser beams [23, 25, 28]. The latter can be created by imparting an azimuthal phase $\Phi(r, \phi) = \ell\phi$, with integer ℓ , to a Gaussian laser beam $E(r) = |E_0| \exp(-r^2/w_0^2)$, where w_0 is the waist. The phase discontinuity at $r = 0$ results in a hollow beam that, for low ℓ , closely approximates a pure $LG_{p=0}^\ell$ mode, where p and ℓ are radial and azimuthal indices. As shown in Figs. 1a-b, a dual ring is produced by introducing a π phase discontinuity at $r = R_c > 0$ such that the resulting beam has large overlap with the $LG_{p=1}^\ell$ mode, which has two radial nodes. The parameter R_c/w_0 controls the modal composition and thus the propagation characteristics. In Ref. [29],

R_c/w_0 was set to generate high purity LG modes. Here, we adjust R_c/w_0 to create a superposition of LG_p^ℓ modes that produces a dark ring at the focus of a lens that is bounded in both the radial and longitudinal directions.

Figure 1c shows the calculated r - z cross-section of a toroidal beam with $\ell = 1$ as it propagates along z through the focus of an $f=215$ mm focal length lens ($w_0 = 1.7$ mm). We have chosen values of R_c such that the barrier heights in the longitudinal and transverse directions are equal. For $\ell=0, 1$, and 2 , this condition is satisfied for $R_c/w_0 \approx 0.71, 0.79$, and 0.85 . The small numerical aperture ($NA=w_0/f=0.008$) leads to a long aspect ratio of $\approx 1:300$ for $\ell = 1$, defined as the ratio of the longitudinal trap frequency ω_{\parallel} to the transverse trap frequency ω_{\perp} . The mode composition is dominated by $p = 0$ (single-ringed) and $p = 1$ (dual-ringed) modes. For $\ell = 0$, *e.g.*, the $p = 0(1)$ fraction is 13%(78%). The potential is harmonic in all directions, as indicated in Fig. 1c. Under these conditions, the ratio of the inner radial barrier height to the outer radial barrier height is ≈ 25 -35%. The radius of the trap depends linearly on ℓ , as it does for hollow beams [30, 31].

The trapping beam is derived from a 30 mW extended cavity diode laser tunable from 776-780 nm. The beam is amplified to ≈ 350 mW with a tapered amplifier of which ≈ 150 mW is coupled into polarization maintaining fiber. The linearly polarized fiber output is collimated with $w_0=1.7$ mm, and reshaped by a 512×512 reflective SLM (Boulder Nonlinear Systems) with $15 \mu\text{m}$ pixels and $\approx 90\%$ absolute diffraction efficiency. A 4 - f imaging setup relays this modified Gaussian beam to a magneto-optical trap (MOT). The 4 - f relay roughly positions the focus of the ring trap over the MOT, but fine longitudinal adjustments are controlled entirely by the SLM by adding a lens phase profile $\Phi_{\text{lens}}(r, \phi) = -\pi r^2/f\lambda$. We compensate for wavefront errors imposed by the SLM by calibrating the programmed phase on a pixel-by-pixel basis.

The experiment begins with a MOT containing 10^7 ^{85}Rb atoms. After a 1 second loading time, the MOT coils are shut off, and the atoms are cooled to $5 \mu\text{K} \approx \hbar\Gamma/60k_B$ during a 10 ms molasses cooling stage. All cooling and trapping beams are then extinguished, followed by a $100 \mu\text{s}$ pulse that optically pumps the atoms into the $F=2$ hyperfine level. The toroidal beam power is ramped to ≈ 150 mW over 5 ms during the molasses stage. This ramp adiabatically loads atoms into the trap and minimizes the energy gained in the loading process. The trap diameter is significantly smaller than the initial MOT size, so we typically load only a small fraction of atoms ($\approx 5 \times 10^4$) into the traps. Collisions with background gas limit the trap $1/e$ lifetimes to ≈ 1 s. After a variable delay, the trapped atoms are imaged onto an electron-multiplying CCD camera (Andor Luca) by a $500 \mu\text{s}$ pulse from the MOT and repump beams. Immediately prior to the imaging pulse, the trapping beam is switched off to avoid Stark shifting of the levels. For linear polarization, the optical potential is [19]

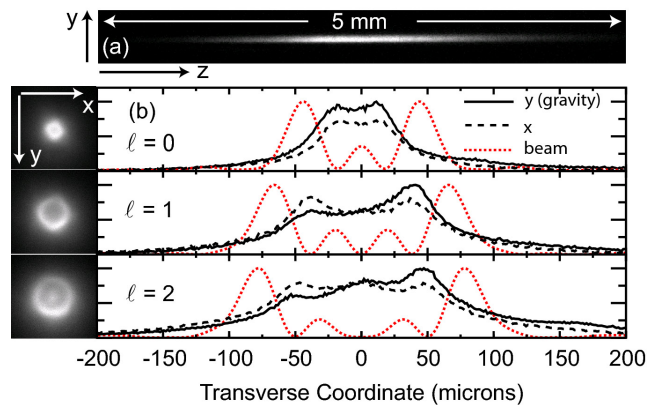


FIG. 2: (Color online) a) Image of atom cloud taken along z -axis for $\ell = 1$. b) Images taken along z -axis (left) and profiles (right) for toroidal traps using $\ell = 0 - 2$. The experimental beam profiles are shown for comparison (dotted line). Trap time for this figure is 600 ms.

$$U(r) = \frac{\hbar\Gamma I(r)}{24I_s} \left(\frac{\Gamma}{\Delta + \Delta_{\text{LS}}} + \frac{2\Gamma}{\Delta} \right) \quad (1)$$

where $I_s=1.6 \text{ mW/cm}^2$ is the saturation intensity, $\Gamma=2\pi \times 6.1 \text{ MHz}$ is the linewidth, and $\Delta_{\text{LS}}=2\pi \times 7.1 \text{ THz}$ ($=15 \text{ nm}$) is the fine structure splitting. The resulting trap depths for $\ell = 1$ and $\Delta = 0.5 \text{ nm}, 1.0 \text{ nm}, 2.0 \text{ nm},$ and 4 nm are $0.26\hbar\Gamma, 0.13\hbar\Gamma, 0.065\hbar\Gamma,$ and $0.033\hbar\Gamma$ (at $780 \text{ nm}, 1 \text{ nm} \leftrightarrow 493 \text{ GHz}$). At $\Delta = 1 \text{ nm}, \omega_{\perp} \approx 2\pi \times 800 \text{ Hz}$ and $\omega_{\parallel} \approx 2\pi \times 3 \text{ Hz}$.

We record images of the trapped atoms with the camera axis along x and along z . Images along x show the longitudinal trap extent (Fig. 2a), while those along z show the toroidal structure (Fig. 2b). The head-on views in Fig. 2b are taken after a trap time of 600 ms for $\ell = 0-2$. Also shown are the azimuthally-averaged beam intensity profiles in the focal plane and atom distributions in the x and y (gravity) directions. Because the trapping beam is propagating horizontally, the potential is not azimuthally symmetric. The gravitational potential energy difference between the intensity nulls for $\ell = 2$ is $\Gamma/30 \approx 2\pi \times 200 \text{ kHz}$ for ^{85}Rb , which is larger than the atom cloud temperature of $2\pi \times 100 \text{ kHz}$. Thus, most atoms are found in the bottom portion of the trap. For $\ell \geq 1$, atoms could initially be loaded on the axis of the beam, along which there is no barrier. This is seen for $\ell = 2$ in Fig. 2. In our configuration it takes a few seconds for these atoms to drift away. Although there should be little interaction between axial atoms and the ring-trapped atoms under adiabatic loading, the axial atoms can be reduced by several means, such as orienting the trapping beam vertically, or loading from an atom distribution that has been dimpled by a blue-detuned Gaussian beam, as in Ref. [1]. A vertical propagation axis would permit a symmetric ring potential in a horizontal plane, but optical access in this direction was limited.

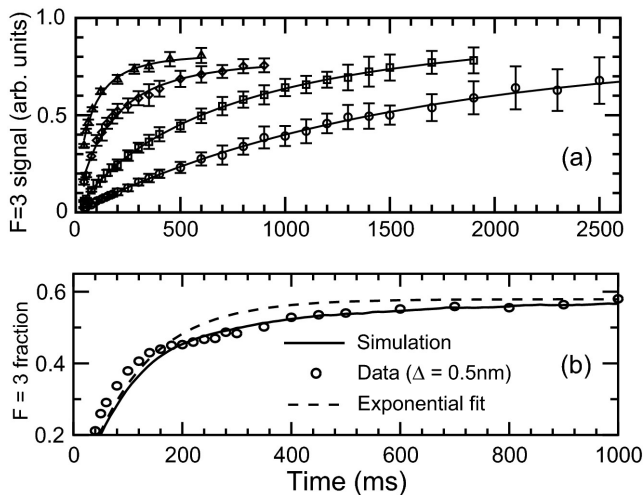


FIG. 3: a) Measurement of $F=3$ fraction as a function of time for $\Delta=0.5$ nm (triangles), 1.0 nm (diamonds), 2.0 nm (squares), and 4.0 nm (circles). Fits (solid lines) using the model described in the text. b) Comparison of 0.5 nm data with a single parameter exponential curve and simulations.

Imaging constraints prevent high contrast images of the toroidal atom distributions. We use an 85 mm Nikon f/1.4 lens, the front element of which is ≈ 250 mm away from the trap location. This lens collects the maximum fluorescence and achieves a peak resolution of ≈ 5 μm but suffers from spherical aberration, which causes the observed loss of contrast.

One benefit of dark traps for coherent atom manipulation is the suppression of photon scattering events [18, 19, 20, 21]. We measure the spin relaxation rate due to Raman scattering by measuring the fraction of atoms in the trap that transfer to $F=3$ as a function of trap [32]. The atoms are first pumped into the $F=2$ hyperfine level. After a variable trapping time, we image only the atoms that transfer to $F=3$ by using a 10 μs pulse of resonant cycling transition light. Within 2 ms, both the repump and the cycling transition beams are switched on to image the atoms in both the $F=2$ and $F=3$ states. For background subtraction, two images with the same pulse sequence are taken with no atoms present. This type of background subtraction is necessary to eliminate false counts due to CCD ghosting. By taking the images during a single loading cycle, the effect of atom number fluctuations is reduced. These images are recorded along x (as in Fig. 2a). Between the first two imaging pulses, the atom distribution expands slightly beyond the few integrated rows of pixels. This leads to a slightly low estimate of the total atom count, but the resulting $F=3$ normalized signal is proportional to the actual $F=3$ fraction.

We record the $F=3$ signal fraction as a function of trap time for four different detunings (Fig. 3a). In the simplest approximation that all atoms have an equal scattering rate, each curve can be modeled by a single exponen-

tial $N_3(t) = C(1 - \exp(-t/\tau))$, as was used in Ref. [18], where τ is the $1/e$ decay time. For $\Delta \leq 1$ nm, however, a single relaxation rate was not observed (Fig. 3b). This difference between our results and those of Ref. [18] is most likely due to differences in the trap loading technique, which we have found to affect the rate curves. We note that the $F=3$ fraction at long times should approach $7/12$, but our measured values are higher due to the pixel integration described above.

Instead of modeling the spin-relaxation with a single-parameter time constant, we phenomenologically “chirp” τ to be $\tau(t) = \tau_0 + \beta t^{1/2}$ so that we can estimate the relaxation rate at different times. We choose a sublinear chirp rate so that the exponential will decay at long times, but the exact functional form will depend on trap geometry. A steadily increasing τ should be expected since atoms initially loaded into the trap in locations of high intensity scatter photons more quickly than those loaded into the dark portions of the trap. Thus, a rapid increase in the $F=3$ fraction is observed for small t , followed by longer relaxation times for the atoms with the least total energy. Using this form for the $F=3$ fraction, approximate spin-relaxation lifetimes at $t = 0$ for $\Delta = 0.5$ nm, 1.0 nm, 2.0 nm, and 4.0 nm are 35 ms, 115 ms, 460 ms, and 1440 ms; after 500 ms, these increase to 140 ms, 230 ms, 750 ms, and 1500 ms.

The scattering time for atoms in a red-detuned trap of comparable depth at $\Delta=0.5$ nm would be ≈ 2.5 ms, which is 50 times shorter than our recorded value. In Ref. [18], the blue-detuned trap had a scattering lifetime 700 times longer than a comparable red-detuned trap at 0.5 nm. That work used significantly higher intensities, where the differences between red- and blue-detuning are more dramatic. Photon scattering may be reduced substantially by using commercially available lasers with higher power and larger detuning. For $\Delta > \Delta_{\text{LS}}$, spin relaxation is further suppressed, asymptotically scaling as Δ^{-4} [32]. The time-dependent scattering rate is likely not limited to toroidal geometries, but to the best of our knowledge, it has been observed for the first time in this report. Also, we point out that we did not directly measure the recoil scattering rate, but for our Δ this is on the same order as the spin-relaxation rate. A recoil scattering rate of 1 s^{-1} corresponds to a heating rate of ≈ 400 nK/s.

To demonstrate the time-dependent scattering rate numerically, we perform Monte Carlo simulations for $\Delta = 0.5$ nm. The simulated trap is ramped on over 5 ms. The atom cloud is initially in the $F = 2$ state and normally distributed in position and velocity to match the MOT size and temperature. Molasses effects are ignored. Within each time step, each atom’s hyperfine level is changed with a probability determined by the local scattering rate, as calculated from the Kramers-Heisenberg formula [32]. The simulation results, compared to data in Fig. 3b, confirm the time-dependent relaxation rate described above. For comparison, the data have been renormalized to have an asymptotic value of $7/12$.

To demonstrate axial confinement and to quantify the

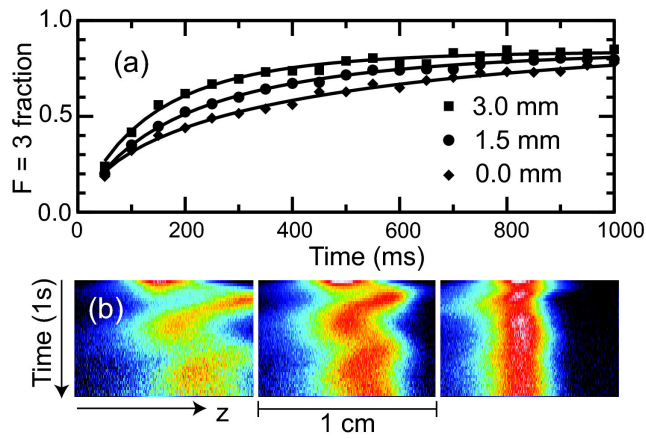


FIG. 4: (Color online) a) Spin-relaxation curves for three different starting positions. b) Images of longitudinal oscillation of the atom cloud using trap displacement from left to right of 3 mm, 1.5 mm, and 0.0 mm.

dependence of the scattering rates on the starting position of the atoms in the trap, we displace the trap minimum from the MOT by adjusting the lens function written to the SLM by a few MOT radii (MOT radius $\approx 250 \mu\text{m}$). Thus, most atoms are initially located in regions of high intensity, reducing the overall scattering lifetime. When the atom cloud is displaced 3 mm, 1.5 mm, and 0.0 mm away from the trap minimum, the single-parameter rate constants (for $\Delta = 1 \text{ nm}$) are 145 ms, 195 ms, and 230 ms (Fig. 4a). For each displacement, we show a composite image of the side views of the trap (Fig 4b), where each row in the image is a different slice in time. These images show the atom cloud oscillating in the longitudinal direction when the trap is not well overlapped with the atom cloud. By displacing the trap focus,

we can also estimate the longitudinal trap frequency. For $\Delta = 1 \text{ nm}$, we measure $\omega_{\parallel} \approx 2\pi \times 2 \text{ Hz}$. This agrees well with the estimate of $\omega_{\parallel} \approx 2\pi \times 3 \text{ Hz}$ from the calculated intensity profiles shown in Fig. 1. The scattering rate data and the composite images can be used to optimize the location of the trap focus, which is done to $\approx 100 \mu\text{m}$ with the SLM.

As with all single-beam traps, the aspect ratio scales with the inverse of the trapping beam NA. For similar beam parameters, an aspect ratio of ≈ 10 could be realized by using a $f = 10 \text{ mm}$ lens. A crossed beam geometry, in which additional beams cap the potential in the longitudinal direction, allows significantly tighter longitudinal confinement and larger diameter traps. In these cases, the ratio R_c/w_0 can be changed for optimal confinement. One possibility is to use values of R_c/w_0 such that the modified beam is primarily in a single $LG_{p=1}^{\ell}$ mode [29]. Pure $LG_{p=1}^{\ell}$ modes have a radial intensity null that persists for all values of z . When R_c/w_0 is chosen such that the most pure $LG_{p=1}^{\ell}$ is formed, the inner radial barrier height is roughly $3\times$ larger than the outer one, and the longitudinal barrier is minimized. Therefore, the crossing beam can be well outside the focal plane, where better beam quality is observed but the ring-shaped null remains dark. The reduction of aberration effects outside the focal plane was shown for hollow beams in Ref. [31].

We have used a spatial light modulator to generate superpositions of LG modes that form single-beam, dark ring traps for cold atoms. We have shown that the atoms can be held in these potentials with long state lifetimes. We have observed atom dynamics in the longitudinal direction and shown that by modifying the trap alignment with the SLM we can optimize the scattering lifetime. This work was funded by the Office of Naval Research and the Defense Advanced Research Projects Agency.

-
- [1] K. Helmerson *et al.*, Nuclear Physics A **790**, 705c (2007).
[2] S. Gupta *et al.*, Phys. Rev. Lett. **95**, 143201 (2005).
[3] P. Jain, A. S. Bradley, and C. W. Gardiner, Phys. Rev. A **76**, 023617 (2007).
[4] Y. V. Bludov and V. V. Konotop, Phys. Rev. A **75**, 053614 (2007).
[5] A. D. Jackson and G. M. Kavoulakis, Phys. Rev. A **74**, 065601 (2006).
[6] I. Lesanovsky and W. von Klitzing, Phys. Rev. Lett. **99**, 083001 (2007).
[7] T. Fernholz *et al.*, Phys. Rev. A **75**, 063406 (2007).
[8] O. Morizot *et al.*, Phys. Rev. A **74**, 023617 (2006).
[9] O. Dutta, M. Jääskeläinen, and P. Meystre, Phys. Rev. A **74**, 023609 (2006).
[10] A. S. Arnold, C. S. Garvie, and E. Riis, Phys. Rev. A **73**, 041606(R) (2006).
[11] S. Wu *et al.*, Phys. Rev. A **70**, 013409 (2004).
[12] J. Ruostekoski and Z. Dutton, Phys. Rev. A **72**, 063626 (2005).
[13] T. L. Gustavson, A. Landragin, and M. A. Kasevich, Class. Quantum Grav. **17**, 2385 (2000).
[14] J. A. Sauer, M. D. Barrett, and M. S. Chapman, Phys. Rev. Lett. **87**, 270401 (2001).
[15] E. M. Wright, J. Arlt, and K. Dholakia, Phys. Rev. A **63**, 013608 (2000).
[16] E. Courtade *et al.*, Phys. Rev. A **74**, 031403(R) (2006).
[17] T. Freearge and K. Dholakia, Opt. Commun. **201**, 99 (2002).
[18] R. Ozeri, L. Khaykovich, and N. Davidson, Phys. Rev. A **59**, R1750 (1999).
[19] R. Grimm, M. Weidemüller, and Y. B. Ovchinnikov, Adv. Atom. Mol. Opt. Phys. **42**, 95 (2000).
[20] N. Friedman, A. Kaplan, and N. Davidson, Adv. Atom. Mol. Opt. Phys. **48**, 99 (2002).
[21] A. Kaplan *et al.*, J. Opt. B: Quantum Semiclass. Opt. **7**, R103 (2005).
[22] T. Kuga *et al.*, Phys. Rev. Lett. **78**, 4713 (1997).
[23] F. K. Fatemi, M. Bashkansky, and Z. Dutton, Opt. Express **15**, 3589 (2007).
[24] S. Bergamini *et al.*, J. Opt. Soc. Am. B **21**, 1889 (2004).

- [25] N. Chattrapiban *et al.*, J. Opt. Soc. Am. B **23**, 94 (2006).
- [26] D. McGloin *et al.*, Opt. Express **11**, 158 (2003).
- [27] V. Boyer *et al.*, Phys. Rev. A **73**, 031402(R) (2006).
- [28] D. P. Rhodes *et al.*, J. Mod. Optics **53**, 547 (2006).
- [29] J. Arlt *et al.*, J. Mod. Optics **45**, 1231 (1998).
- [30] J. E. Curtis and D. G. Grier, Phys. Rev. Lett. **90**, 133901 (2003).
- [31] F. K. Fatemi and M. Bashkansky, Appl. Opt. **46**, 7573 (2007).
- [32] J. D. Miller, R. A. Cline, and D. J. Heinzen, Phys. Rev. A **47**, R4567 (1993).